catalysts

MDPI

Article

Air Regeneration of Ethanol-Laden Pellet NaY-SiO_2 and Pt/NaY-SiO_2: Effects of Air Flow Rate on Pt Morphology and Regeneration Efficiency

Cheng-Yang Yeh [1], Yi-Ting Chen [1], Nan-Yu Chen [2] and Jen-Ray Chang [1,*]

[1] Department of Chemical Engineering, National Chung Cheng University, Chia-Yi 62102, Taiwan; d703561@hotmail.com (C.-Y.Y.); tinanzste@gmail.com (Y.-T.C.)
[2] National Synchrotron Radiation Research Center, Hsinchu 30076, Taiwan; Chen.ny@nsrrc.org.tw
* Correspondence: chmjrc@ccu.edu.tw; Tel.: +886-5-2729123

Received: 19 June 2018; Accepted: 12 July 2018; Published: 17 July 2018

Abstract: Regeneration process and adsorbent performance were investigated by a fixed-bed adsorber at 300 °C. Surface species, zeolite structure, and Pt morphology were characterized by FT-IR, XRPD and EXAFS, respectively. Performance test results indicated that ethanol adsorption capacity of Pt/NaY-SiO_2 is about 2.5 times that of NaY-SiO_2. After regeneration, adsorption-capacity loss is 2.5 and 43%, respectively, for Pt/NaY-SiO_2 regenerated at superficial velocity of 13.2 ($PtR_{(HF)}$) and 5.3 cm/min ($PtR_{(LF)}$); in contrast, it is 8 and 21%, respectively, for $NaYR_{(HF)}$ and $NaYR_{(LF)}$. The appearance of absorption bands in the CH stretching region (υ_{CH}) of the IR spectra characterizing the regenerated NaY-SiO_2 suggested that the adsorption-capacity loss for NaY-SiO_2 was mainly caused by the deposition of carbonaceous species formed in regeneration, which cannot be burned off readily at 300 °C. In contrast, no υ_{CH} bands have been observed for the IR spectra of $PtR_{(HF)}$ and $PtR_{(LF)}$, indicating that Pt helps to burn off carbonaceous species. However, Pt agglomeration was observed in TEM and EXAFS for Pt/NaY-$SiO_{2(LF)}$. The appearance of a υ_{CO} band at about 2085 cm^{-1} of the IR spectra characterizing $PtR_{(LF)}$ suggested that Pt agglomeration was induced by CO adsorption. The growth of Pt particles decreases the ethanol adsorbed on Pt together with the conversion of ethanol to ethoxides and aldehyde, leading to a decrease of adsorption capacity.

Keywords: catalytic adsorbent; NaY zeolite; regeneration; X-ray absorption fine structure; CO-induced Pt aggregation

1. Introduction

The effluents from industrial processes often contain VOCs (volatile organic compounds), which pose a threat to human health and the environment [1–3]. For low VOC concentration cases, a three-step process can be used [4]. In this process, the VOCs are first concentrated by adsorption at low temperature until the breakthrough occurs. The adsorbent is regenerated by passing a small quantity of air or other gas to generate a VOC concentrated process stream, which is converted to innocuous CO_2 in an incinerator. To improve the process, catalytic components can be added to promote both adsorption and incineration, and the process steps are integrated into a single reactor. In the integrated catalytic/adsorption process, fixed bed reactors containing catalytic adsorbents are employed to continuously adsorb VOCs from the effluents in one bed and convert VOCs on the catalytic adsorbent into benign carbon dioxide and water in the other [5–7]. Compared with the conventional adsorber-incinerator, the system is relatively simple, high in VOC removal efficiency, and low in operation and maintenance cost. However, for the catalytic/adsorption process, extra fuel input for air regeneration is still necessary and is a key criterion for assessing the process efficiency.

In order to reduce the use of extra fuel, the catalytic adsorbent should have dual functions, which serves to adsorb VOCs rapidly and oxidize the adsorbed VOCs catalytically and completely at modest temperatures. In addition, the catalytic adsorbent should be hydrothermally stable to allow repeated adsorption and regeneration cycles [8].

NaY-SiO_2 extrudate was used as an adsorbent and was prepared by blending NaY powder with silica gel, and followed with kneading, extruding and calcination [9]. NaY zeolite was chosen because: (1) this material is non-flammable with high thermal stability, allowing high-temperature regeneration; (2) the surface area is high (>500 m^2/g), which allows metal or metal oxides to be dispersed on the surface, thereby enhancing catalytic oxidation activity; and (3) Na form zeolite may suppress the formation of coke precursors during the regeneration [9–11]. Noble metals, such as Pt, have catalytic oxidation activity for VOC [7,11–15] and were incorporated into NaY-SiO_2 by means of impregnation techniques to prepare the catalytic adsorbents.

In the previous paper, the goals were to investigate the effects of Pt on the adsorption performance of Pt/NaY-SiO_2 and explain how Pt enhances the adsorption capacity while decreasing the adsorption rate [14]. The experimental results indicated that the adsorption capacities of NaY-SiO_2 in removing ethanol from water-containing air stream are greatly enhanced by the addition of Pt and the active Pt clusters on NaY play the main roles in catalytically converting the adsorbed ethanol to ethoxides and aldehyde. Those Pt-adsorbed species could spill over to displace sodium and acid site bound water, leaving the Pt clusters for further adsorption, and thus increasing ethanol adsorption capacity.

In the regeneration, the air flow rate is the key parameter. The flow rate has to be sufficient so as to: (1) supply enough oxygen for combustion; (2) minimize the resistance of component transfer; (3) carry away the heat generated to prevent overheating the bed and to form a sharp moving combustion band; and (4) to prevent the morphology change of catalytic adsorbents and the corresponding performance-deterioration. Hence, the goals of this study are to study the effects of flow rate on the regeneration performance and to investigate the roles of Pt in increasing regeneration efficiency. Moreover, the importance of sufficient air in successful regeneration and how air supply in regeneration affects Pt morphology will be reported as well.

An empirical model was used to describe experimental breakthrough curves, and the parameters of the model were used to access the regeneration efficiency. The surface-bound species in regeneration were characterized by DRIFT (diffuse-reflectance infrared Fourier transform). The morphology of Pt clusters, the oxidized Pt species formed in regeneration, and the interactions between Pt and support were characterized by EXAFS (extended X-ray absorption fine structure) spectroscopy. The characterization results combined with the parameters estimated from the model were used to rationalize the change of Pt morphology in regeneration and its corresponding effects on regeneration efficiency.

EXAF measurements performed in transmission mode present a much higher signal-to-noise ratio than those in fluorescence mode; thus, high Pt–Pt shell contributions, oxidation of Pt, and Pt–support interactions would not be affected significantly by noise. To facilitate EXAF study, a high Pt precursor dosage of 1 wt. % was used to prepare Pt/NaY-SiO_2, so that EXAF can be measured in transmission mode [16]. However, because of the rather high metal loading, Pt clusters are more likely to be aggregated. For industrial application, noble metal loading is designed to provide sufficient catalytic oxidation activity to ensure no carbon residue deposited on the catalytic adsorbent even after the deterioration of adsorption capacity due to the destruction of the zeolite frameworks with several regeneration cycles. Hence, optimal Pt loading should be investigated further.

2. Results and Discussion

2.1. Performance Tests

The dynamics of fixed-bed adsorption (breakthrough curve) for the fresh and air-regenerated NaY-SiO_2 and Pt/NaY-SiO_2 are shown in Figures 1 and 2, respectively. The stoichiometric dynamic

adsorption capacity was calculated by integrating the area above the whole breakthrough curve. The results indicated that the adsorption capacity of NaY-SiO_2 was decreased 8 and 21% after the 300 °C regeneration at high (v_s = 13.2 cm/min) and low flow rates (v_s = 5.3 cm/min), respectively; the samples were noted as $NaYR_{(HF)}$ and $NaYR_{(LF)}$, respectively, for high and low flow rates. The adsorption capacity was only decreased 2.5% for Pt/NaY-SiO_2 regenerated at high flow rate ($PtR_{(HF)}$), whereas it was 43% at low flow rate ($PtR_{(RF)}$).

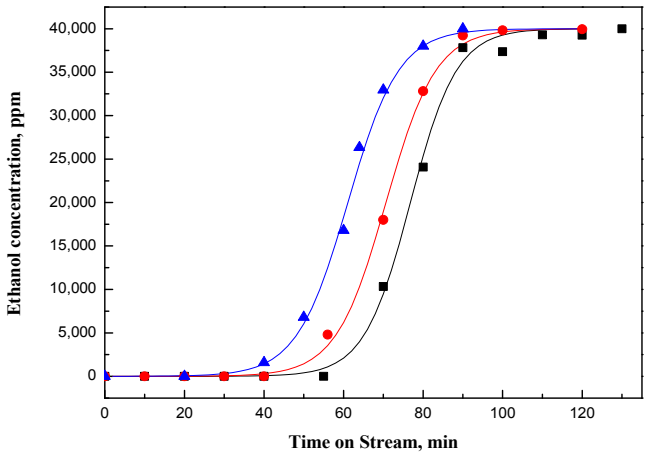

Figure 1. Breakthrough curves of ethanol for fresh NaY-SiO_2 (■), $NaYR_{(HF)}$ (●), and $NaYR_{(LF)}$ (▲); the solid line in the figure is the data calculated from Equation (4) with the parameters shown in Table 1.

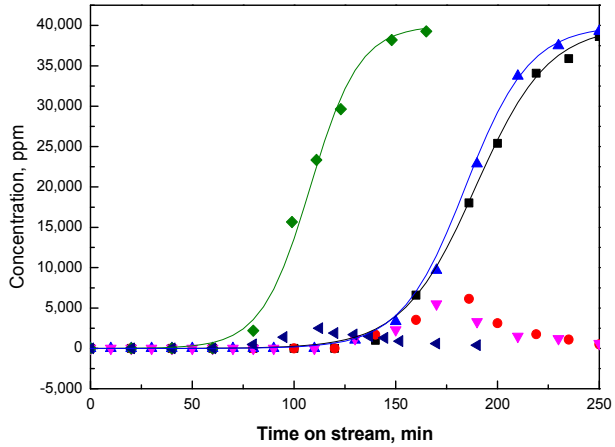

Figure 2. Ethanol breakthrough curve (■) and acetaldehyde formed in the test (●) for fresh Pt/NaY-SiO_2; ethanol breakthrough curve (▲) and acetaldehyde formed (▼) for $PtR_{(HF)}$; ethanol breakthrough curve (♦) and acetaldehyde formed (◄) for $PtR_{(LF)}$.

As shown in Figure 1, only ethanol was detected for NaY-SiO_2. In contrast, for Pt/NaY-SiO_2, both ethanol and a small amount of acetaldehyde were detected at the end of the adsorption cycle (Figure 2). Acetaldehyde is formed from the oxidative dehydrogenation of ethanol catalyzed by Pt clusters. Much lower acetaldehyde formation was detected for $PtR_{(LF)}$, as opposed to that for $PtR_{(HF)}$ and for fresh Pt/NaY-SiO_2, suggesting loss of Pt activity in low-flow-rate air regeneration.

During the performance tests, the adsorption/reaction zone moves through the adsorber bed; adsorbent is saturated behind the adsorption/reaction zone and is free of adsorbate in front of the zone. The length of the adsorption/reaction (A/R) zone is a function of the mass transfer rate of the ethanol adsorbate from the gas stream to the active sites of the catalytic adsorbent and is represented by the steepness of breakthrough curve. In cases where the mass-transfer rate is decreased,

the adsorption/reaction zone broadens and the breakthrough curve becomes less steep. As shown in Figures 1 and 2, the breakthrough curve for Pt/NaY-SiO_2 is not as steep as that for NaY-SiO_2, indicating that other steps were involved besides ethanol adsorption when Pt is present. Reported in our previous paper, ethanol could be adsorbed on Pt clusters first, catalytically dissociated to ethoxide, and then diffused the adsorbed ethanol and/or ethoxide to the adsorption sites of NaY [14]. Since all these steps take time, the mass transfer rate for Pt/NaY-SiO_2 is thus lower than that for NaY-SiO_2.

As shown in Figure 2, the adsorption capacity and mass transfer rate of $PtR_{(HF)}$ are close to those of the fresh Pt/NaY-SiO_2, while the adsorption capacity of $PtR_{(LF)}$ is lower but the mass transfer rate is slightly higher (Figure 2). The results are consistent with the loss of Pt activity for $PtR_{(LF)}$ suggested by the decrease of acetaldehyde formed in the catalytic adsorption process.

2.2. Model for Breakthrough Curve

In order to assess the effects of air flow rate on the efficiency of regeneration quantitatively, a model for breakthrough curves was proposed. The differential material balance for a fixed adsorption bed is formulated as:

$$-D_l\frac{\partial^2 C}{\partial z^2}+u\frac{\partial C}{\partial z}+\frac{\partial C}{\partial t}+\frac{\rho_p(1-\varepsilon)}{\varepsilon}\frac{\partial q}{\partial t}=0 \quad (1)$$

$$t=0,\ q_r=q^0,\ z=0,\ C=C^0 \quad (2)$$

In Equation (1), D_l ($cm^2 \cdot s^{-1}$) is axial dispersion coefficient; ε is bed void fraction; c (mg/cm^3) is gas phase adsorbate concentration in bulk flow; z (cm) is axial distance; u ($=v_s/\varepsilon$, cm/s) is interstitial velocity; t (min) is elapsed time; ρ_p (g/cm^3) is apparent adsorbent density, and q (mg adsorbate/g adsorbent) is the adsorption capacity per unit mass of adsorbent [17,18].

In addition, the rate of mass transfer across the pellet (dq/dt) is equal to ethanol adsorbed on the catalytic adsorbents and is formulated by an empirical equation, $\partial q/\partial t = \eta ka C(q0 - q)$; where C is ethanol concentration in gas phase, q is adsorption capacity, $q0$ is stoichiometric adsorption capacity, ka is adsorption constant, and η is a ratio of adsorption rates with component transfer resistance to adsorption rate without resistance [14].

Since the characteristic time, t, for adsorbate moving from the bed inlet to the outlet is much longer than the residence time of the transporting gas stream, L/u (L: length of adsorption bed), pseudo-steady-state approximation, $\partial C/\partial t = 0$, was assumed for Equation (1). Because L/d_p in this study is about 50, the axial dispersion term of Equation (1) is set at zero. After neglecting the unsteady and axial dispersion terms, Equation (1) can then be directly integrated [19]. The analytical solution is given as:

$$\frac{C(z,t)}{C^0}=\frac{\exp\left(\eta k_a C^0 t\right)}{\exp\left(\frac{\eta k_a q^0 \rho_p z}{u_s}\right)+\exp(\eta k_a C^0 t)-1},\ u_s=\frac{\varepsilon}{(1-\varepsilon)}u \quad (3)$$

Since the exponential terms in Equation (3) are much greater than (1), the equation can be further simplified as:

$$\frac{C(L,t)}{C^0}\approx\frac{\exp(\tau t)}{\exp(\xi)+exp(\tau t)},\ \xi=\frac{\eta k_a q^0 \rho_p L}{u_s},\ \tau=\eta k_a C^0 \quad (4)$$

The stoichiometric adsorption capacity (q^0) was used to evaluate the efficacy of regeneration, while η was used to characterize diffusion limitation. Since Ka is a constant, lumped ηKa can thus be used to evaluate the relative component transfer resistance before and after regeneration, although we were unable to decouple η and Ka.

The parameters in Equation (4) were estimated by fitting the breakthrough curves with least-squares method, and the results are summarized in Table 1.

Table 1. Ethanol adsorption capacities and effectiveness factor obtained from breakthrough curves.

Adsorbent	τ, 1/min	ξ	q^0, mg/g	(η × k_a), L/mg·min
NaY-SiO_2	0.172	13.21	57.8	2.29
$NaYR_{(HF)}$	0.158	11.25	53.4	2.10
$NaYR_{(LF)}$	0.163	9.94	45.8	2.17
Pt/NaY-SiO_2	0.0573	10.84	142.2	0.76
$PtR_{(HF)}$	0.0627	11.58	138.7	0.83
$PtR_{(LF)}$	0.0831	8.97	81.1	1.11

Note: Adsorbent samples were tested at 38 °C with total GHSV of 450 h^{-1} in flowing 40,000 ppm of ethanol with 700 ppm water moisture in air.

2.3. Regeneration Tests

As shown in Figure 3a,b, Pt catalytically oxidizes the surface species on NaY-SiO_2; hence, the total amount of CO_2 evolved from Pt/NaY-SiO_2 is about 6 times that from NaY-SiO_2 for both high and low air flow rate (Table 2). There are two peaks appearing in the CO_2 evolved spectra of $PtR_{(HF)}$ and $PtR_{(LF)}$. The results suggest at least two different kinds of species on Pt/NaY-SiO_2. The peak appearing at low temperature (about 150 °C for $PtR_{(HF)}$) could be attributed to the oxidation of ethanol and acetaldehyde, while that at high temperature (300 °C) could be the characteristic peak of the combustion of carbon residue, which were formed from the oligomerization of ethanol-derivative species, such as ethylene and crotonaldehyde, conversion of acetone to mesityl oxide, and hydrocarbon decomposition [20,21]. Ethylene could be formed from dehydration of ethanol catalyzed by BrØnsted acid sites inside NaY and/or the decomposition of diethylether (DEE) [22]. Crotonaldehyde could be formed from aldol condensation of two molecules of acetaldehyde, which was formed from the dehydrogenation of ethanol. Acetone could be produced through aldol condensation of acetate, which could be formed by the oxidation of acetaldehyde [20]. In our previous study, characteristic peaks of ethoxides species have been detected by IR and EXAFS further suggested the coordination of ethoxide with Pt clusters via bridging hydrogen of ethanol ($Pt^HOC_2H_5$) [14]. Inferred from the paper reported by Ferencz et al., carbon was suggested to be formed from the decomposition of Pt–bound CH_3 species, presumably, through acetaldehyde and acetyl species [20].

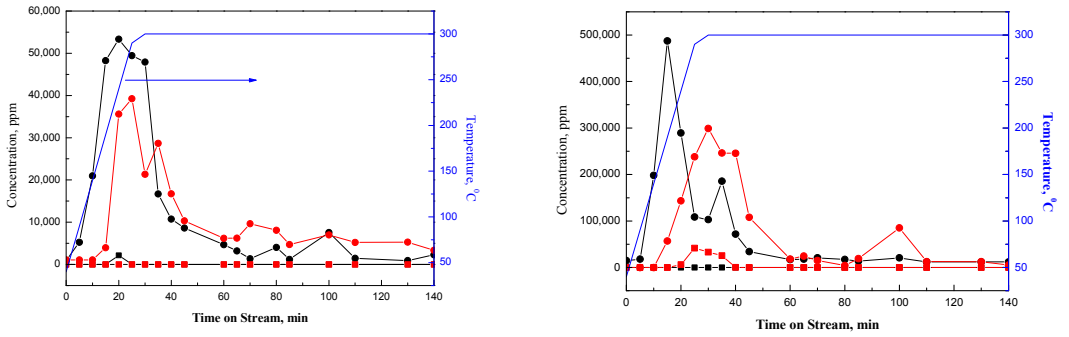

(**a**) (**b**)

Figure 3. (**a**) CO_2, CO formed in temperature programmed regeneration of EtOH-laden NaY-SiO_2: CO_2 formed at high flow rate (black •), CO_2 formed at low flow rate (red •), CO formed at high flow rate (black ■), CO formed at low flow rate (red ■); blue line solid line in the figure is the setting temperature. (**b**) CO_2, CO formed in temperature programmed regeneration of EtOH-laden Pt/NaY-SiO_2: CO_2 formed at high flow rate (black •), CO_2 formed at low flow rate (red •), CO formed at high flow rate (black ■), CO formed at low flow rate (red ■).

The oxidation of ethanol in regeneration was strongly influenced by air flow rate. As shown in Figure 3b, the peak characterizing the oxidation of ethanol is shifted from 150 °C to about 290 °C and the total amount of CO_2 decreased by about 60% when superficial velocity was decreased from 13.2 to 5.3 cm/min (Table 2). In addition, a significant number of partial oxidation species, CO, were also formed at a low flow rate besides CO_2; in contrast, only trace amounts of CO were detected at a high flow rate (Figure 3b).

Concomitant with the oxidation of the adsorbed ethanol, ethanol and ethanol-derivative species were desorbed from Pt/NaY-SiO_2 and NaY-SiO_2. The main ethanol-derivative species for Pt/NaY-SiO_2 is acetaldehyde, and that for NaY-SiO_2 is diethylether (DEE). In our previous paper [9], protonated ethanol ($C_2H_5OH_2^{\delta+}$) was detected in FT-IR spectroscopy characterizing ethanol adsorbed on NaY-SiO_2 at room temperature. Inferring from the literature that the protonated ethanol is more susceptible to elimination or substitution reaction [22], we suggested that DEE could be catalytically formed from the reaction of the protonated ethanol on NaY with undissociated ethanol during air regeneration. Ethylene could thus be produced by ethanol dehydration and/or DEE cracking. However, this could be due to quick oligomerization and/or strong adsorption, no significant amount of ethylene was detected in the effluent gas.

Based on the carbon balance calculated from the breakthrough curve (Figure 1) and profiles of evolved species (Figures 3a and 4a), about 22 and 38% of ethanol-derivative species (Table 2) were estimated to be deposited on NaY-SiO_2 after air regeneration at high and low flow rates, respectively. These strongly adsorbed carbon residues are defined as coke. The paraffinic coke could be formed from the ethylene oligomerization and aromatics from cyclization followed by hydrogen transfer reactions [21,23].

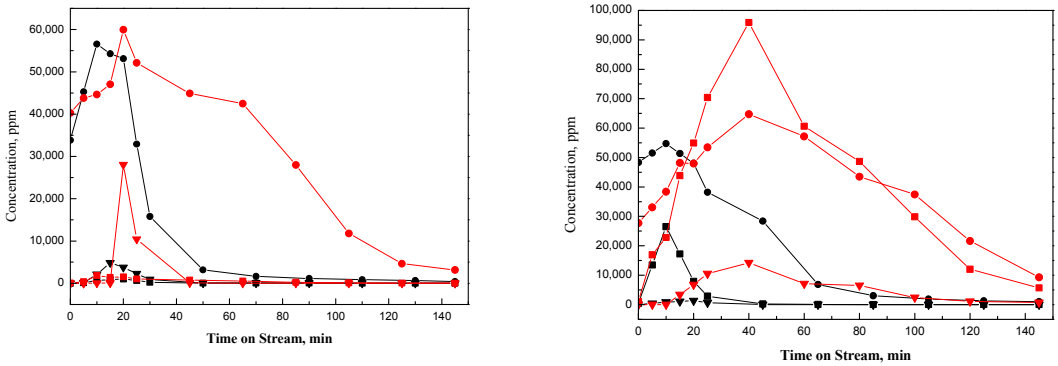

Figure 4. (**a**) Ethanol desorbed and species formed in temperature programmed regeneration of EtOH-laden NaY-SiO_2: ethanol desorbed at high flow rate (black ●), ethanol desorbed at low flow rate (red ●), DEE formed at high flow rate (black ▼), DEE formed at low flow rate (red ▼); acetaldehyde formed at high flow rate (black ■), acetaldehyde formed at low flow rate (red ■). (**b**) Ethanol desorbed and species formed in temperature programmed regeneration of EtOH-laden Pt/NaY-SiO_2: ethanol desorbed at high flow rate (black ●), ethanol desorbed at low flow rate (red ●), acetaldehyde formed at high flow rate (black ■), acetaldehyde formed at low flow rate (red ■), DEE formed at high flow rate (black ▼), DEE formed at low flow rate (red ▼).

Table 2. Ethanol desorption and total oxidation capacities obtained from ethanol desorption and CO_2 formation profiles in air regeneration.

Adsorbent	Desorption mg/g	Total Oxidation mg/g
NaYR$_{(HF)}$	30.8	14.0
NaYR$_{(LF)}$	30.9	6.0
PtR$_{(HF)}$	46.2	84.7
PtR$_{(LF)}$	91.0	35.0

Total oxidation, partial oxidation, dehydration, and desorption of the adsorbed ethanol are the competitive processes occurring in air regeneration. The addition of Pt to NaY-SiO_2 increases the oxidation rate and thus decreases the amount of ethanol desorption (Figure 4a,b). In addition, instead of DEE formed on NaY-SiO_2, acetaldehyde was formed from the dehydrogenation of Pt–associated ethoxy-group; as shown in Figure 4b, only trace DEE was detected in high flow rate regeneration. However, this could be due to insufficient air supply for oxidative dehydrogenation reaction; small amounts of DEE were also detected in low flow rate regeneration of Pt/NaY-SiO_2.

For pure NaY-SiO_2, ethanol is adsorbed on the BrØnsted acid site to form a hydrogen-bonded ethanol monomer ($C_2H_5OH_2^{\delta+}$). This hydrogen-bonded monomer then reacts with an oncoming ethanol to form DEE directly (Figure 5a). The monomer intermediate could also adsorb the oncoming ethanol to form ethanol dimer, which indirectly produces DEE by elimination of water molecule (Figure 5b) [22].

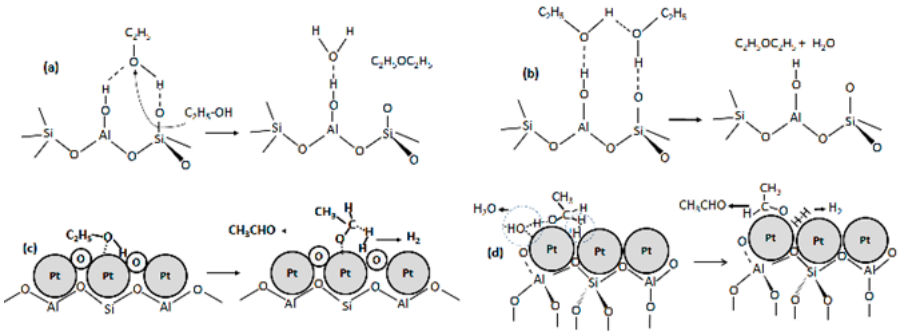

Figure 5. Reaction mechanisms of (**a**) DEE formed on NaY-SiO_2 via hydrogen bonded monomer, (**b**) DEE formed on NaY-SiO_2 via ethanol dimer intermediate, (**c**) acetaldehyde formed on platinum oxides of Pt/NaY-SiO_2, and (**d**) acetaldehyde formed on platinum of Pt/NaY-SiO_2.

Oxidative dehydrogenation of ethanol to acetaldehyde via ethoxy species may require the oxide surface to acquire a negative charge or hydroxyl group to abstract hydrogen from ethanol. For Pt/NaY-SiO_2 regenerated at high flow rate with sufficient oxygen, surface platinum-oxide was detected by EXAFS (Section 2.5). The oxide with negative charge facilitates the adsorption of ethanol, which dissociates heterolytically to yield an ethoxide bound to Pt and a proton bond to oxide (Figure 5c). The surface Pt–bound ethoxide intermediate then was dehydrogenated to acetaldehyde [24,25]. In contrast, for regeneration at low flow rate, no significant surface platinum-oxide species have been detected by EXAFS (Section 2.5). In this case, Pt clusters could be oxidized to form transient surface Pt–O, which catalytically dehydrogenate ethanol to form acetaldehyde. This transient Pt–O was quickly reduced by H_2 and/or CO in insufficient oxygen conditions, so that no Pt–O could be observed using EXAFS. The acetaldehyde could also be formed via the abstraction of hydrogen from Pt bound ethanol, $Pt^HOC_2H_5$, to form ethoxide intermediate, followed by abstraction of hydride from the ethoxide intermediate. The hydride was associated with surface proton to form hydrogen molecules (Figure 5d) [26].

In the presence of platinum, the affinity of ethanol to Pt–O may be higher than that to NaY, resulting in a shift of reaction toward oxidative dehydrogenation. However, when oxygen supply is insufficient, some of ethanol was adsorbed on NaY and dehydrated to produce DEE.

2.4. Characterization of Surface Species on NaY-SiO_2 and Pt/NaY-SiO_2 by FT-IR

There is residual coke deposited on the regenerated NaY-SiO_2, as shown by the IR spectra (Figure 5a), consistent with lower adsorption capacity of the regenerated *NaY-SiO_2*.

The presence of absorption bands in the CH stretching region of paraffinic groups (3000–2800 cm^{-1}) after in situ air treatment of EtOH–laden NaY-SiO_2 (Figure 6A) indicated the formation of coke on $NaYR_{(HF)}$ and $NaYR_{(LF)}$ [27]. In contrast, no absorption bands in this region being observed for Pt/NaY-SiO_2 suggests the roles of Pt in inhibiting coke formed on Pt/NaY-SiO_2 during regeneration. Since dehydration reactions and combustion (oxidation) reaction are competitive reactions in air regeneration, combustion of ethanol catalyzed by Pt minimizes the formation of coke precursors together with oligomerization reactions. In addition, facilitated by exothermic heat associated with the ethanol combustion, coke formed on NaY-SiO_2 can be catalytically oxidized to CO_2 quickly.

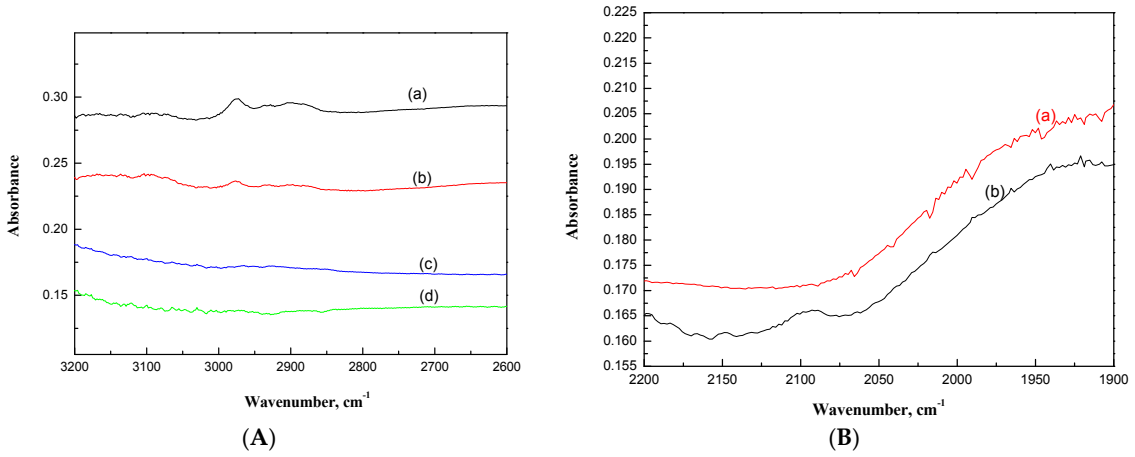

Figure 6. (**A**) FT-IR spectra of carbonaceous species formed on (a) $NaYR_{(LF)}$, (b) $NaYR_{(HF)}$, (c) $PtR_{(LF)}$, (d) $PtR_{(HF)}$. (**B**) FT-IR spectra of the υ_{CO} stretching region characterizing CO adsorbed on (a) $PtR_{(HF)}$, (b) $PtR_{(LF)}$.

There were no aromatic-coke characteristic absorption bands in the range between 3000 and 3200 cm^{-1} observed, suggesting that cokes formed on NaY-SiO_2 are mostly paraffinic (Figure 6A) [27]. The absorption bands at 2974 cm^{-1} and 2842 cm^{-1} were assigned to asymmetric stretching (ν_{sym}) and symmetric vibration (ν_{asym}), respectively, for CH_3, and the absorption bands at 2930 cm^{-1} (ν_{sym}) and 2894 cm^{-1} (ν_{sym}) were assigned to ν_{sym} and ν_{asym}, respectively, for CH_2. As shown in Figure 5a, band intensities in the CH stretching region (3000–2800 cm^{-1}) decreased with increasing air flow rate, whereas the relative intensity between CH_3 and CH_2 (I_{CH3}/I_{CH2}) did not vary significantly. Since I_{CH3}/I_{CH2} is an indication on the chain length of the carbonaceous species, the results suggested that increasing air flow rate in regeneration reduces carbonaceous species formation due to the increase of thermal combustion reaction (Table 2) but does not affect chain propagation reaction.

Regeneration of Pt/NaY-SiO_2 showed the formation of CO in addition to CO_2 at low flow rate, while only trace CO was observed at high flow rate (Figure 6B). As expected, no characteristic peaks in the region of carbonyl stretching (υ_{CO}) were observed for $PtR_{(HF)}$ (Figure 6B). In contrast, the υ_{CO} characteristic peak at 2085 with a shoulder at 2100 cm^{-1} was observed for $PtR_{(LF)}$ (Figure 6B). CO molecules have a stretching frequency of 2143 cm^{-1}. The shift of the peak to a lower frequency for $PtR_{(LF)}$ suggests the adsorption of CO on Pt clusters. When CO is adsorbed on Pt clusters, electron

back-donation transfer occurs from the d-orbital of Pt to anti-bonding $2\pi^*$ orbital of the linearly coordinated CO molecule leading to a decrease of carbon-oxygen bond order together with υ_{CO} frequency [28].

The band peaking at 2085 cm^{-1} is the same as that for CO adsorbed on Pt/NaY at room temperature reported in the literature [29]. The shift of the CO absorption bands to higher frequencies for the shoulder (2100 cm^{-1}) may be due to the interaction of foreign gases, O_2, with the chemisorbed CO. This effect was attributed to a decrease of the electron density at the Pt surface, which decreased the back-donation from the metal to the CO π^* orbital, and thus increased the υ_{CO} frequency [30].

2.5. Effects of Air Flow Rate on the Structure of Pt/NaY-SiO$_2$

Even though the regeneration temperature (300 °C) is far lower than the zeolite damage temperature (600 °C) [31], the NaY framework might be destroyed due to hot spot and water formed in the combustion reaction. Hence, XRPD was used to examine any thermal destruction of NaY in air regeneration.

The comparison of synchrotron XRPD patterns for fresh Pt/NaY-SiO_2, $PtR_{(HF)}$, and $PtR_{(LF)}$ are shown in Figure 7. Since there are no significant differences in XRPD patterns between fresh Pt/NaY-SiO_2, $PtR_{(HF)}$, and $PtR_{(LF)}$, the results indicate that NaY structure was intact after regeneration; in other words, regeneration flow rate has no effects on zeolite frameworks. Lower adsorption capacity for $PtR_{(LF)}$ should be attributed to other factors and Pt-morphology change was expected to be the most possible one. Since the Pt crystal size is too small to be characterized by synchrotron XRPD, the morphology of Pt clusters, as well as Pt–support interactions, were then characterized by EXAFS.

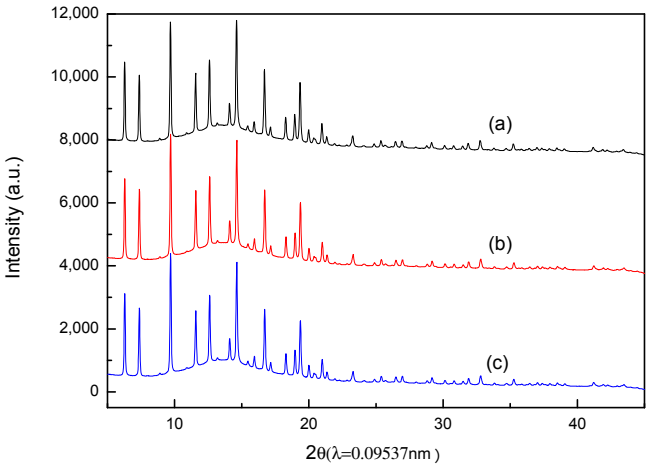

Figure 7. Powder X-ray spectra of (a) fresh Pt/NaY-SiO_2, (b) $PtR_{(HF)}$, (c) $PtR_{(LF)}$.

As shown in Figure 8, the k^3-weighted Pt–Pt phase- and amplitude-corrected Fourier transforms show peaks appearing at 2.7, 3.9, 4.7, and 5.7Å, consistent with the metal-metal distance of bulk Pt clusters; k^3-weighted Fourier transform minimizes low-Z (Z is atomic number) contributions, such as Pt–O; hence, the appearance of Pt–Pt characteristic peaks was not influenced by these contributions [16].

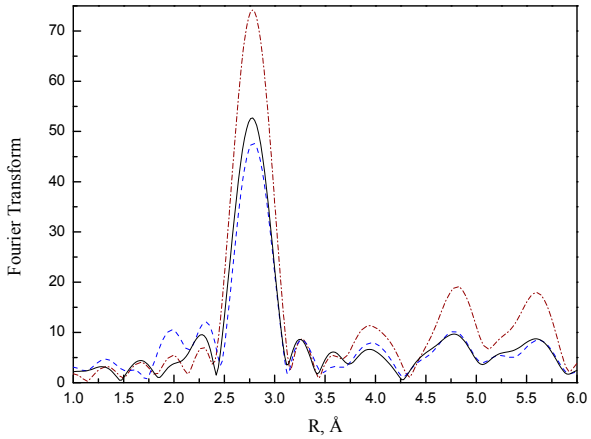

Figure 8. Magnitude of the EXAFS Fourier transform ($3.5 < k^3 < 14.0$, Pt–Pt phase and amplitude corrected) for (a) fresh Pt/NaY-SiO_2 (black solid line), (b) $PtR_{(HF)}$ (blue dash line), (c) $PtR_{(LF)}$ (brown dot-dashed line).

The Pt–Pt characteristic peak intensities for fresh Pt/NaY-SiO_2 are lower than those for $PtR_{(LF)}$, while they are slightly higher than $PtR_{(HF)}$. Since the amplitude of the Fourier transformed EXAFS function reflects the metal particle size [16,32], the higher amplitude intensity for $PtR_{(LF)}$ suggests Pt sintering at low flow-rate regeneration. The results were confirmed by TEM images; as show in Figure 9a,c, the comparison of TEM images between Pt/NaY-SiO_2 and $PtR_{(LF)}$ clearly shows that the average Pt particle size of $PtR_{(LF)}$ is much bigger than that of Pt/NaY-SiO_2. In contrast, TEM images of Pt/NaY-SiO_2 and $PtR_{(HF)}$ were difficult to differentiate. The results suggested that the lower amplitude intensity of $PtR_{(HF)}$ (Figure 8) was attributable to the loss of Pt–Pt contribution caused by the formation of oxidic Pt species. With sufficient oxygen, surface Pt atoms could be oxidized concomitantly with the combustion reaction. The formation of oxidic Pt in high flow rate regeneration was confirmed by analyzing low-Z contributions of EXAFS.

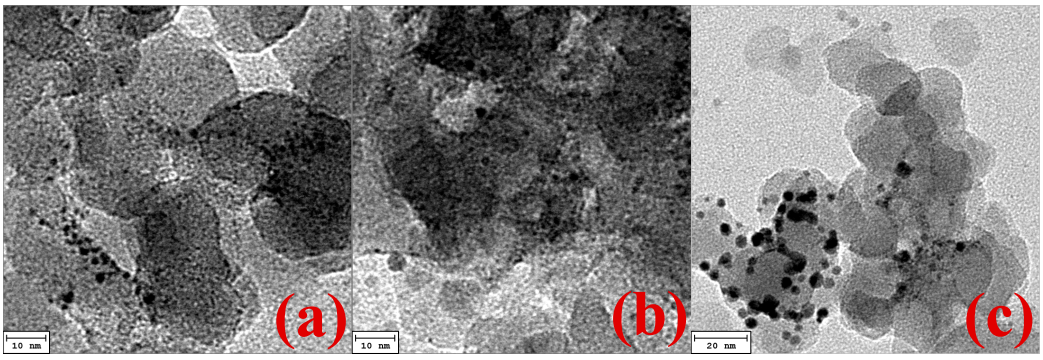

Figure 9. TEM images for Pt cluster deposited on (**a**) Pt/ NaY-SiO_2, (**b**) $PtR_{(HF)}$, (**c**) $PtR_{(LF)}$.

A normal k^2 ($2.68 < k < 14.3$ $Å^{-1}$)-weighted Fourier transformation without correction was performed and the major contributions ($Pt–Pt_{1st\ shell}$ + Pt–O) were isolated by inverse Fourier transformation in the range $1.73 < r < 3.32$ Å. With the difference technique, a Pt–Pt was calculated and then subtracted from the isolated data. A Pt–Pt contribution was calculated that agreed as well as possible with the experimental results in the high k range ($7.0 < k < 14.0$ $Å^{-1}$); the low-Z contributions in this range are small. After the subtraction, the residual spectrum was expected to represent the contributions from Pt oxides and/or Pt–support interactions.

For the fresh Pt/NaY-SiO_2, the imaginary of Pt–O phase-corrected Fourier transform of the residual spectra displayed a peak at 2.1–2.2 Å (Figure 10). This peak was assigned to the interactions

between platinum and zeolite oxygen [33,34]. In comparison with the residual spectrum of fresh Pt/NaY-SiO_2, a broad peak with shorter bond distance appears at 2.0–2.1 Å for $PtR_{(HF)}$. The broad peak could be a lumped peak contributed by α–PtO_2 with a Pt–O bond distance of 2.05 Å [35] and Pt–support interactions.

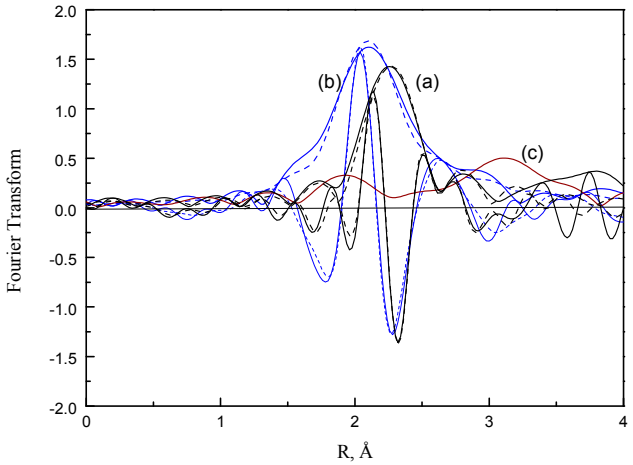

Figure 10. Comparison of the EXAFS Fourier transform ($3.5 < k^3 < 12.0$, Pt–O phase corrected) of residual EXAFS spectra between: (a) fresh Pt/ NaY-SiO_2 (black), (b) $PtR_{(HF)}$ (blue), (c) $PtR_{(LF)}$ (brown); magnitude (solid line), imaginary (dashed line).

As opposed to the residual spectra of $PtR_{(LF)}$ and fresh Pt/NaY-SiO_2, the intensity of the residual spectrum for $PtR_{(LF)}$ is much smaller, suggesting that oxidic Pt species formed on $PtR_{(LF)}$ are insignificant. In addition, because the Pt–O contribution for $PtR_{(LF)}$ is rather small and is greatly interfered with by noise, parameter estimation for this contribution was not attempted.

The structural parameters of fresh Pt/NaY-SiO_2 and $PtR_{(HF)}$ were estimated by a nonlinear least-squares multiple-shell fitting routine [36]. The structural parameters are listed in Table 3 and the comparisons of experimental and calculated Pt–O are shown in Figure 10.

Table 3. Summary of EXAFS analysis results.

Shell	N	R (Å)	$1000 \times \Delta\sigma^2$ ($Å^2$)	ΔE_0 (eV)
		EtOH.Pt-NaY		
Pt–O	0.7 ± 0.1	2.17 ± 0.01	1 ± 1	-16 ± 1
Pt–Pt	7.4 ± 0.2	2.77 ± 0.01	3 ± 1	-2 ± 1
		$PtR_{(HF)}$		
Pt–O	2.2 ± 0.1	2.06 ± 0.01	9 ± 1	-6 ± 1
Pt–Pt	6.4 ± 0.1	2.76 ± 0.01	3.6 ± 0.2	-4.3 ± 0.1
		$PtR_{(LF)}$		
Pt–Pt	10.4 ± 0.1	2.76 ± 0.01	5.0 ± 0.1	-2.1 ± 0.1

Note: N, the coordination number for the absorber-backscatterer pair; R, the average absorber-backscatterer distance; $\Delta\sigma^2$, the difference in Debye-Waller factors between sample and standard; ΔE_0, the inner potential correction.

After air regeneration at high flow rate, the average Pt–O bond distance decreased from 2.17 to 2.06 Å, the coordination number increased from 0.8 to 2.2, and the Pt–Pt coordination number decreased from 7.4 to 6.4 (Table 3), confirming the oxidation of Pt clusters concomitant with the combustion of ethanol and its derivatives. In contrast, after regeneration at low flow rate, the Pt–Pt coordination

number increased from 7.4 to 10.4. These results, combined with the increase of higher Pt–Pt shell intensity (Figure 8), suggest the growth of Pt clusters with morphology resembling bulk Pt.

The average Pt particle size on NaY-SiO_2 determined by the use of first-shell Pt–Pt coordination number ($CN_{Pt–Pt}$) of EXAFS measurements [37] is 1.3 and 3.3 nm, respectively, for fresh Pt/NaY-SiO_2 and $PtR_{(LF)}$, while that determined from TEM images is about 1.5 and 3.8 nm, respectively (Figure 9a,c). The larger Pt particle size determined by TEM could be because: (1) the coupling between CN and the relative Debye-Waller factor ($\Delta\sigma$) of EXAFS equation causes the inherent uncertainty of coordination numbers (CN) estimation; and (2) Pt clusters with sizes less than 1 nm are difficult to resolve by TEM [38].

Oxidic Pt species were formed in Pt clusters during air regeneration with high flow rate. Because the formation of these oxidic species decreases Pt–Pt contributions, we are unable to estimate Pt particle size by the use of the correlation of $CN_{Pt–Pt}$ with particle size reported in literature [37]. However, it is shown in TEM images that the average Pt particle size of $PtR_{(HF)}$ is close to that of fresh Pt/NaY-SiO_2 (Figure 9a,b), suggesting that only few or no Pt clusters were aggregated in high flow regeneration.

2.6. Effects of Air Supply Rate on Regeneration Efficiency

For efficient and complete regeneration of the adsorbent, adequate supply of oxygen is necessary. Based on stoichiometry calculation, without desorption, it takes about 45.6 mmole O_2 per 5 g of ethanol-laden Pt/NaY-SiO_2 adsorbent. Besides total oxidation, partial oxidation, and ethanol desorption also took placed in air regeneration. In high flow rate regeneration, an air supply of 61.2 mmole is enough for ethanol total oxidation; notwithstanding sufficient oxygen supply, about one-third of ethanol was desorbed from Pt/NaY-SiO_2, concomitant with total oxidation. However, in low flow rate regeneration, corresponding to low air supply (24.5 mmole) and low partial pressure of oxygen, more ethanol was desorbed, more acetaldehyde was produced, and some CO was also formed. The formation of CO greatly deteriorates regeneration efficiency.

The mechanism for the aggregation of Pt clusters remains to be elucidated. However, CO co-adsorbed on Pt clusters, besides O_2 in the regeneration at low flow rate, suggests a role of CO adsorption. When CO is adsorbed on less stable (smaller) Pt clusters, back-donation effects may lead to a decrease in Pt–support interactions. Consequently, the affinity of this mobile CO-adsorbed Pt species for more stable (larger) Pt clusters may be greater than that of the mobile Pt species to support. The decreased metal–support interactions lift migrating Pt clusters, causing them to float over the support [39]. The enhancement of surface diffusivities due to floating of Pt clusters promotes the coalescence of Pt clusters. The CO-adsorption-assisted Ostwald ripening [40] induces the change of Pt morphology, characterized by the coalescence of Pt clusters in 3-dimensional (Figure 8).

In our previous paper, we reported that ethanol bonds to bulk fcc Pt clusters of Pt/NaY-SiO_2 through bridging hydrogen [14]. Facilitated by the adsorption heat, some of the adsorbed ethanol molecules, $Pt^{H}OC_2H_5$, were converted to ethoxide and acetaldehyde in breakthrough performance tests. In comparison with ethanol, these ethanol-converted species could have higher affinity for NaY-SiO_2, and thus could spill over to displace sodium and acid site-bound water and leave the Pt clusters for further adsorption. This catalytic adsorption property of Pt leads to an increase of adsorption capacity. The aggregation of Pt clusters in the regeneration at low flow rate, however, deteriorates the catalytic adsorption function of Pt, leading to a decrease of adsorption capacity.

3. Materials and Methods

3.1. Preparation of PtO_2/NaY and NaY Pellet

Impregnation technique was used to prepare NaY-supported PtO_2 (PtO_2/NaY) powder. Zeolite powder (Sodium Silicoaluminate, Na_2O:Al_2O_3:5.0 SiO_2:xH_2O, GRACE Davison) of 60 g was put in a flask and pretreated by heating to 120 °C under vacuum. Platinum salt solution was prepared by dissolving 1.92 g $H_2PtCl_6.6H_2O$ (Uni region Bio-Tech) in 44.6 g de-ionized water. The solution was

then added dropwise while shaking the vacuum flask. The slurry was then dried in vacuum at 150 °C for 2 h and calcined in air at 450 °C for 4 h. The resulting material was noted as PtO_2/NaY powder. To make pellet PtO_2/NaY, a silica powder of 30 g (T600, PPG Industries) was mixed with a 3 N nitric acid solution to form a silica colloid. 60 g PtO_2/NaY powders were placed in a bowl of a small kneader. The blades of the kneader were rotated while the small portions of the silica colloid were being added to cause the powder to be converted to a paste. The paste was extruded from an extruder to make cylinder extrudate of 2 mm in diameter. The PtO_2/NaY extrudate were then cut to form pellets of about 6 mm in length. The pellets were pre-dried at 120 °C for 8 h to remove water and calcined under air at 450 °C for 4 h. The resulting pellet sample was noted as PtO_2/NaY-SiO_2. The same procedure was used to prepare pellet NaY (NaY-SiO_2).

3.2. Performance Tests

The dynamics of fixed-bed adsorption for PtO_2/NaY-SiO_2 and NaY-SiO_2 were performed in a stainless-steel tube with an inside diameter of 2.2 cm and length of 45 cm. The reactor was heated electrically and temperature controlled by a PID temperature controller with three *K*-type thermal couples at the outer wall of the reactor. The reactor was packed with 5.0 g adsorbents mixed with inert ceramic (sphere of about 2.0–5.0 mm diameter) in a ratio of 1:10 by volume, and a gradient packing method was used so that the adsorbent bed would have a nearly uniform temperature in air regeneration and the wall and bypassing effects would be minimized. Prior to adsorption tests, NaY-SiO_2 were heated in flowing air (50 mL/min, volumetric flow rate) at 150 °C for 1 h. For PtO_2/NaY-SiO_2, the sample was pre-reduced by treatment with H_2 at 300 °C for 1 h and was noted as Pt/NaY-SiO_2. After the samples were cooled down to room temperature (about 35 °C), performance tests were carried out. The total flow rate of the reaction mixture (78 mg of ethanol with 0.52 mg water moisture in L of air) was 50 mL/min. Mass flow controllers (AeraFC-7700C) were used for accurate and stable control of gas flow rates. Effluents from the reactor were collected and analyzed by use of GC periodically.

After the saturation, the ethanol-laden adsorbents were regenerated by heating the adsorption bed with a ramping rate of 10 °C/min to 300 °C and maintained for 2 h in flowing air. In order to study the effects of air flow rate on regeneration efficiency, air superficial velocity (v_s), defined as volumetric flow rate of that fluid divided by the cross-sectional area of adsorption column, was set at 13.2 (high flow rate) and 5.3 cm/min (low flow rate), respectively. The NaY-SiO_2 regenerated at high flow rate was notes as $NaYR_{(HF)}$, and that at low flow rate $NaYR_{(LF)}$.

The performance of the regenerated Pt/NaY-SiO_2 and NaY-SiO_2 were tested by the same steps as those of the fresh one. For X-ray absorption spectroscopy measurements, Pt/NaY-SiO_2 samples after air regeneration were purged with N_2 for 2 h. After N_2 purge, the regenerated samples were removed from the adsorption column and transferred to a dry box for storage. The samples regenerated at high and low flow rates were noted as $PtR_{(HF)}$ and $PtR_{(LF)}$, respectively.

The GC used for analysis of ethanol and its secondary products was a Shimadzu Model GC-14B equipped with a capillary column (length: 60 m; ID: 0.32 mm; Film: 0.5 μm; stationary phase: HP-INNOWAX, Restek Corp., Bellefonte, PA, USA) and an FID detector. The column was operated at 40 °C to 200 °C with ramping rate of 10 °C/min and a flow rate of 50 mL/min of dry He. Oxidation species, CO and CO_2, were analyzed by GC-14B equipped with a unibead-packed column of 3 m × 3 mm i.d. and a TCD detector.

3.3. Synchrotron XRPD

Powder X-ray diffraction was performed at the BL01C2 beamline of the National Synchrotron Radiation Research Center (NSRRC, Hsinchu, Taiwan), with the wavelength of 0.9535 Å (13.0 keV). The ring of NSRRC was operated at energy 1.5 GeV with a typical current 300 mA with top-up injection mode. The synchrotron X-ray was produced from a 5.0 T superconducting wavelength shift magnet. Beyond the prefocusing mirror, a double crystal monochromator, which used the Si (111) plane to

yield the monochromatic beam, was followed by a refocusing toroidal mirror. The sample was sealed in the capillary. During the X-ray exposure, the sample was kept at fast spin in order to increase the orientations of powders. Two-dimensional diffraction patterns were recorded by a Mar345 imaging plate system, with a sample-to-detector distance of 300 mm. Diffraction angle was calibrated with silver Behenate and Si powders (NBS640b) standards. One-dimensional XRPD (X-ray powder diffraction) profiles were integrated from selected fan-like areas of the symmetrical 2-D powder rings using the Fit2D program [41].

3.4. Characterization of Catalyst Samples by Infrared Spectroscopy

Diffuse reflectance infrared Fourier transform spectra (DRIFT) characterizing ethanol adsorbed on the catalytic adsorbents were recorded with a Shimadzu IR Prestige-21 (Kyoto, Japan), equipped with an MCT detector. The cell was connected to a vacuum/gas-handling manifold for in situ treatment. The pellet samples were crushed and made into powder. For PtO_2/NaY-SiO_2, the powder sample was reduced by flowing H_2 at 300 °C for 1 h. For NaY-SiO_2, the sample was pretreated by flowing air at 150 °C for 1 h. After the pretreatments, the samples were cooled to room temperature, and then air (flowing at 10 mL/min at 1 atm) containing 40,000 ppm ethanol and 7000 ppm (mole) water was introduced into the cell and maintained for about 1 h. After the saturation of ethanol adsorption, air with a superficial velocity of about 13 and 5 cm/min, respectively, was introduced into the cell. The cell was heated to 300 °C with ramping rate of 10 °C/min and maintained for about 2 h. After the samples were cooled to room temperature, the cell was evacuated to a pressure of about 0.1 to 1 torr and IR spectra with a 2 cm^{-1} spectral resolution were recorded.

3.5. X-ray Absorption Spectroscopy

All X-ray absorption spectra of Pt L_{III} edge (11,564 eV) were measured on the beam line BL17C at the Synchrotron Radiation Research Center (SRRC) in Hsinchu, Taiwan, with storage ring energy 1.5 GeV and a beam current between 120 and 200 mA. A Si (111) double-crystal monochromator was employed for energy selection, and mirrors rejected higher harmonic radiation. The transmission geometry was arranged using gas-filled ionization chambers to monitor the intensities of the incident and transmitted X-ray beams. For fresh Pt/NaY-SiO_2, PtO_2/NaY-SiO_2 pellets were pulverized, pressed into wafer, and loaded in to the EXAFS cell, allowing treatment in flowing gases prior to the measurement. The reduction conditions were exactly the same as those for performance tests.

For $PtR_{(HF)}$ and $PtR_{(LF)}$, the samples were also pulverized and pressed into wafer in a dry box, and then transferred and loaded into the EXAFS cell in a N_2-filled glove bag.

A full spectrum for the Pt L_{III} absorption edge was obtained over energy levels from 11,364 to 12,764 eV. To ensure reliability of the spectra, Pt metal foil was also monitored to evaluate the stability of the energy scale for each measurement. Data reduction and data analysis were performed with the XDAP code developed by Vaarkampet et al. [42]. Standard procedures were used to extract the EXAFS data from the measured absorption spectra. The pre-edge was approximated by a modified Victoreen curve [16,43] and the background was subtracted using cubic spline routines [16]. Normalization was performed by dividing the data by the height of the absorption edge at 50 eV above the edge [16,42]. The EXAFS contributions for Pt–Pt were analyzed with phase shifts and backscattering amplitudes obtained from EXAFS data for Pt foil. Pt–O were analyzed with phase shifts and backscattering amplitudes calculated from FEFF8 [44].

4. Conclusions

The EXAFS and FT-IR results suggest that ethanol on Pt/NaY-SiO_2 appears to be adsorbed catalytically, and proceeds through ethoxide to aldehyde. Those Pt adsorbed species could spill over to displace sodium and acid site bound water, leaving the Pt clusters for further adsorption, and thus increase ethanol adsorption capacity to about 2.5 times that of NaY-SiO_2 [14]. Moreover, in comparison with NaY-SiO_2, Pt/NaY-SiO_2 offers higher VOC destructive efficiency in air regeneration. During

air regeneration, long-chain paraffinic coke was formed on NaY-SiO_2, leading to lower regeneration efficacy. In contrast, the species adsorbed on Pt/NaY-SiO_2 were catalytically oxidized to CO_2 and H_2O at high flow rate (v_s = 13.2 cm/min); the adsorption capacity loss after regeneration was 2.5% for Pt/NaY-SiO_2, in contrast to 8% for NaY-SiO_2. However, despite the fact that reducing air flow rate in regeneration is an effective way to decrease auxiliary-fuel utilization, aggregation of Pt clusters was observed in low-flow-rate regeneration (v_s = 5.3 cm/min). Hence, for industrial application, regeneration efficiency loss caused by the Pt aggregation should be taken into account in exploring the optimal regeneration conditions. Mesoporous silica materials might be useful for adsorbing VOCs, specifically, for large molecule. Trapping Pt clusters in the pores of mesoporous material, instead of the deposition of Pt on silica binder and/or the external surface of NaY particles, may confine Pt clusters in pores during regeneration and thus suppress the aggregation of Pt clusters. In addition, Pd–Pt bimetallic interactions may help Pt to anchor on zeolite or mesoporous materials, thereby, inhibiting Pt migration in regeneration. For long-term commercial operation, sufficient air supply to minimize CO-induced Pt aggregation should be employed. Moreover, optimal Pt loading and/or oxychlorination-redispersion [39] should be considered to ensure no coke is deposited on the catalytic adsorbent even after the destruction of the zeolite frameworks with several regeneration cycles.

Author Contributions: C.-Y.Y. and Y.-T.C. prepared catalytic adsorbent samples and performed regeneration and breakthrough tests; Y.-T.C. wrote rough-draft manuscript in Chinese; C.-Y.Y. analyzed regeneration and breakthrough curve data; N.-Y.C. performed synchrotron and EXAFS experiments and did preliminary data analysis of EXAFS; J.-R.C. analyzed EXAFS data, organized experimental data, and wrote manuscript.

Acknowledgments: The EXAFS data were analyzed using the FEFF and XDAP Data Analysis Program. XDAP program was developed by M. Vaarkam; J. C. Linders, and D. C. Koningsberger. The supports of Ministry of Science & Technology, R.O.C. (Contract No. MOST-106-2221-E-194-054), National Synchrotron Radiation Research Center (NSRRC), and Refining & Manufacturing Research Institute, CPC Corporation, Taiwan are acknowledged.

Conflicts of Interest: The authors declare no conflict of interest.

References

1. Kampa, M.; Castana, E. Human health effects of air pollution. *Environ. Pollut.* **2008**, *151*, 362–367. [CrossRef] [PubMed]
2. Hasana, N.H.; Saidb, M.R.; Lemanc, A.M. Health effect from Volatile Organic Compounds and Useful Tools for Future Prevention: A Review. *Int. J. Environ. Eng. Sci. Technol. Res.* **2013**, *1*, 28–36.
3. Woodruff, T.J.; Caldwell, J. Estimating cancer risk from outdoor concentrations of hazardous air pollutants in 1990. *Environ. Res.* **2000**, *82*, 194–206. [CrossRef] [PubMed]
4. Ueda, K.; Takata, Y.; Shibahara, T.; Yoshida, Y. Method for Treating Gas and Regenerating Catalyst Portion by Portion. U.S. Patent 5,254,512, 19 October 1993.
5. Teller, A.J. Integrated Catalytic/Adsorption Process for Destroying Volatile Organic Compounds. U.S. Patent 6,051,199, 18 April 2000.
6. Kullavanijaya, E.; Trimm, D.L.; Cant, N.W. Adsocat: Adsorption/catalytic combustion for VOC and odour control. *Stud. Surf. Sci. Catal.* **2000**, *130*, 569–574.
7. Tomatis, M.; Xu, H.H.; He, J.; Zhang, X.D. Recent Development of Catalysts for Removal of Volatile Organic Compounds in Flue Gas by Combustion: A Review. *J. Chem.* **2016**, *2016*, 1–16. [CrossRef]
8. Yan, T.Y.; Chang, J.-R. Process for Removing Volatile Organic Compounds. U.S. Patent 7,060,236 B2, 13 June 2006.
9. Chen, N.-Y.; Liu, M.-C.; Yang, S.-C.; Chang, J.-R. Structure and surface properties of NaY-SiO_2 pellets investigated by synchrotron radiation XRPD and FT-IR: impact of silica binder. *Ind. Eng. Chem. Res.* **2015**, *54*, 8456–8468. [CrossRef]
10. Meininghaus, C.K.W.; Prins, R. Sorption of volatile organic compounds on hydrophobic zeolites. *Microporous Mesoporous Mater.* **2000**, *35*, 349–365. [CrossRef]
11. Avgouropoulos, G.; Oikonomopoulos, E.; Kanistras, D.; Ioannides, T. Complete oxidation of ethanol over alkali-promoted Pt/Al_2O_3 catalysts. *Appl. Catal. B* **2006**, *65*, 62–69. [CrossRef]

12. Tsou, J.; Magnoux, P.; Guisnet, M.; Órfão, J.J.M.; Figueiredo, J.L. Catalytic oxidation of volatile organic compounds (VOCs) oxidation of methyl-isobutyl-ketone over Pt/zeolite catalysts. *Appl. Catal. B* **2005**, *57*, 117–123. [CrossRef]
13. Gluhoi, A.C.; Bogdanchikova, N.; Nieuwenhuys, B.E. Total oxidation of propene and propane over gold-copper oxide on alumina catalysts comparison with Pt/Al_2O_3. *Catal. Today* **2006**, *113*, 178–181. [CrossRef]
14. Liu, M.-C.; Hsieh, C.-C.; Lee, J.-F.; Chang, J.-R. Impact of Pt and V_2O_5 on ethanol removal from moist air using pellet silica-bound NaY. *Ind. Eng. Chem. Res.* **2015**, *54*, 8678–8689. [CrossRef]
15. Mihai, O.; Creaser, D.; Olsson, L. Adsorption and Oxidation Investigations over Pt/Al_2O_3 Catalyst: A Microcalorimetric Study. *Catalysts* **2016**, *6*, 73–84. [CrossRef]
16. Koningsberger, D.C.; Prins, R. *X-ray Absorption: Principles, Applications, Techniques of EXAFS, SEXAFS, and XANES*; Wiley: New York, NY, USA, 1988; pp. 321–373.
17. Chu, K.H. Fixed bed sorption: Setting the record straight on the Bohart-Adams and Thomas models. *J. Hazard. Mater.* **2010**, *177*, 1006–1012. [CrossRef] [PubMed]
18. Bezverkhyy, I.; Bouguessa, K.; Geantet, C.; Vrinat, M. Adsorption of tetrahydrothiophene on faujasite type zeolites: Breakthrough curves and FTIR spectroscopy study. *Appl. Catal. B* **2006**, *62*, 299–305. [CrossRef]
19. Bohart, G.S.; Adams, E.Q. Some aspects of the behavior of charcoal with respect to chlorine. *J. Am. Chem. Soc.* **1920**, *42*, 523–544. [CrossRef]
20. Ferencz, Z.; Erdohelyi, A.; Baán, K.; Oszkó, A.; Óvári, L.; Kónya, Z.; Papp, C.; Steinrück, H.-P.; Kiss, J. Effects of Support and Rh Additive on Co-Based Catalysts in the Ethanol Steam Reforming Reaction. *ACS Catal.* **2014**, *4*, 1205–1218.
21. Mattos, L.V.; Jacobs, G.; Davis, B.H.; Noronha, F.B. Production of Hydrogen from Ethanol: Review of Reaction Mechanism and Catalyst Deactivation. *Chem. Rev.* **2012**, *112*, 4094–4123. [CrossRef] [PubMed]
22. Kadama, S.A.; Shamzhy, M.V. IR Operando study of ethanol dehydration over MFI zeolite. *Catal. Today* **2018**, *304*, 51–57. [CrossRef]
23. Madeira, F.F.; Gnep, N.S.; Magnoux, P.; Maury, S.; Cadran, N. Ethanol transformation over HFAU, HBEA and HMFI zeolites presenting similar Bronsted acidity. *Appl. Catal. A* **2009**, *367*, 39–46. [CrossRef]
24. Shinohara, Y.; Satozono, H.; Nakajima, T.; Suzuki, S.; Mishima, S. Study of the Interaction of Ethanol with the Broensted and Lewis Acid Sites on Metal Oxide Surfaces Using the DV-Xa Method. *J. Chem. Softw.* **1997**, *4*, 41–49. [CrossRef]
25. Idriss, H.; Seebauer, E.G. Reactions of ethanol over metal oxides. *J. Mol. Catal. A Chem.* **2000**, *152*, 201–212. [CrossRef]
26. Mallat, T.; Baiker, A. Oxidation of Alcohols with Molecular Oxygen on Solid Catalysts. *Chem. Rev.* **2004**, *104*, 3037–3058. [CrossRef] [PubMed]
27. Pinard, L.; Hamieh, S.; Canaff, C.; Madeira, F.F.; Batonneau-Gener, I.; Maury, S.; Delpoux, O.; Tayeb, K.B.; Pouilloux, Y.; Vezin, H. Growth mechanism of coke on HBEA zeolite during ethanol transformation. *J. Catal.* **2013**, *299*, 284–297. [CrossRef]
28. Cotton, F.A.; Wilkinson, G. *Advanced Inorganic Chemistry*, 5th ed.; John Wiley & Sons: New York, NY, USA, 1988; pp. 58–68.
29. Rades, T.; Borovkov, V.Y.; Kazansky, V.B.; Polisset-Thfoin, M.; Fraissard, J. Diffuse Reflectance IR Study of CO Adsorption on a Bimetallic Pt–Pd Catalyst Supported on NaY Zeolite. Evidence of Alloy Formation. *J. Phys. Chem.* **1996**, *100*, 16238–16241. [CrossRef]
30. Little, L.H. *Infrared Spectra of Adsorbed Species*; Academic Press: New York, NY, USA, 1966; pp. 47–62.
31. Breck, D.W. *Zeolite Molecular Sieves*; John Wiley & Sons, Inc.: New York, NY, USA, 1974; pp. 492–496.
32. Iwasawa, Y. *X-ray Absorption Fine Structure for Catalysts and Surface*; World Scientific: Singapore, 1995; pp. 173–189.
33. Koningsberger, D.C.; Gates, B.C. Nature of the metal-support and metal-promoter interface: implications of X-ray absorption spectroscopy for catalysis. *Catal. Lett.* **1992**, *14*, 271–277. [CrossRef]
34. van Zon, J.B.A.D.; Koningsberger, D.C.; van't Blik, H.F.J.; Sayers, D.E. An EXAFS study of the structure of the metal-support interface in highly dispersed Ph/Al_2O_3 catalysts. *J. Chem. Phys.* **1985**, *82*, 5742–5754. [CrossRef]
35. Pedersen, T.M.; Liab, W.X.; Hammer, B. Structure and activity of oxidized Pt(110) and α-PtO_2. *Phys. Chem. Chem. Phys.* **2006**, *8*, 1566–1574. [CrossRef] [PubMed]

36. Varrkamp, M. *XDAP User's Guide*; XAFS Services International: Utrecht, The Netherlands, 1996.
37. Marinković, N.S.; Sasaki, K.; Adtić, R.R. Nanoparticle size evaluation of catalysts by EXAFS: Advantages and limitations. *Zaštita Materijala* **2016**, *57*, 101–109. [CrossRef]
38. Shih, C.-C.; Chang, J.-R. Genesis and growth of platinum subnano-particles on activated-carbon characterized by X-ray absorption spectroscopy: effects of preparation conditions. *Mater. Chem. Phys.* **2005**, *92*, 89–97. [CrossRef]
39. Horsley, J.A. *Stability of Supported Catalysts: Sintering and Redispersion*; Cataltica Studies Division: Mountain View, CA, USA, 1991; pp. 11–85, 305–316.
40. Berkó, A.; Szökő, J.; Solymosi, F. Effect of CO on the morphology of Pt nanoparticles supported on TiO_2 (1 1 0)-(1 × n). *Surf. Sci.* **2004**, *566–568*, 337–342. [CrossRef]
41. Hammersley, A.P. *FIT2D V12.012 Reference Manual V6.0*; ESRF Internal Report, ESRF98HA01T; ESRF: Grenoble, France, 2004.
42. Vaarkamp, M.; Linders, J.C.; Koningsberger, D.C. A new method for parameterization of phase shift and backscattering amplitude. *Physica B* **1995**, *208–209*, 159–160. [CrossRef]
43. Vaarkamp, M.; Dring, I.; Oldman, R.J.; Stern, E.A.; Koningsberger, D.C. Comparison of theoretical methods for the calculation of extended X-ray-absorption fine structure. *Phys. Rev. B* **1994**, *50*, 7872–7883. [CrossRef]
44. Zabinsky, S.I.; Rehr, J.J.; Ankudinov, A.R.; Albers, C.; Eller, M.J. Multiple-scattering calculations of X-ray-absorption spectra. *Phys. Rev. B* **1995**, *52*, 2995–3009. [CrossRef]